

Contents lists available at ScienceDirect

Tectonophysics

journal homepage: www.elsevier.com/locate/tecto



1D-velocity structure and seismotectonics of the Ecuadorian margin inferred from the 2016 Mw7.8 Pedernales aftershock sequence



Sergio León-Ríos^{a,*}, Hans Agurto-Detzel^b, Andreas Rietbrock^{a,c}, Alexandra Alvarado^d, Susan Beck^e, Phillipe Charvis^f, Benjamin Edwards^c, Yvonne Font^f, Tom Garth^g, Mariah Hoskins^h, Colton Lynner^e, Anne Meltzer^h, Jean Matthieu Nocquet^{f,i}, Marc Regnier^f, Frederique Rolandone^{f,j}, Mario Ruiz^d, Lillian Soto-Cordero^h

- ^a Geophysical Institute, Karlsruhe Institute of Technology, 76187 Karlsruhe, Germany
- ^b Geoazur, Université Côte d'Azur, IRD, CNRS, Observatoire de la Côte d'Azur, Géoazur, Valbonne, France
- ^c School of Environmental Sciences, University of Liverpool, Liverpool L69 3GP, UK
- d Instituto Geofísico Escuela Politécnica Nacional, Ladrón de Guevara E11-253 Andalucía, Quito 170525, Ecuador
- e Department of Geosciences, University of Arizona, 1040 East 4th Street, Tucson, AZ 85721, USA
- ^f Université Côte d'Azur, IRD, CNRS, Observatoire de la Côte d'Azur, Géoazur, Valbonne, France
- ⁸ Department of Earth Sciences, University of Oxford, South Parks Road, Oxford OX1 3AN, UK
- ^h Department of Earth and Environmental Sciences, 1 West Packer Avenue, Lehigh University, Bethlehem, PA 18015, USA
- ⁱ Institut de Physique du Globe de Paris, Sorbonne Paris Cité, Université Paris Diderot, UMR 7154 CNRS, Paris, France
- ^j Sorbonne Université, CNRS-INSU, ISTeP UMR 7193, Paris, France

ARTICLE INFO

Keywords: 2016 Pedernales earthquake Ecuador Velocity model Subduction zone Regional moment tensor Aftershock sequence

ABSTRACT

On April 16th 2016 a Mw 7.8 earthquake ruptured the central coastal segment of the Ecuadorian subduction zone. Shortly after the earthquake, the Instituto Geofisico de la Escuela Politecnica Nacional of Ecuador, together with several international institutions deployed a dense, temporary seismic network to accurately categorize the post-seismic aftershock sequence. Instrumentation included short-period and broadband sensors, along with Ocean Bottom Seismometers. This deployment complemented the permanent Ecuadorian seismic network and recorded the developing aftershock sequence for a period of one year following the main-shock. A subset of 345 events with $M_L > 3.5$, were manually picked in the period of May to August 2016, providing highly accurate Pand S-onset times. From this catalogue, a high-quality dataset of 227 events, with an azimuthal gap $< 200^{\circ}$, are simultaneously inverted for, obtaining the minimum 1D velocity model for the rupture region, along with hypocentral locations and station corrections. We observe an average Vp/Vs of 1.82 throughout the study region, with relatively higher Vp/Vs values of 1.95 and 2.18 observed for the shallowest layers down to 7.5 km. The high relative Vp/Vs ratio (1.93) of the deeper section, between 30 km and 40 km, is attributed to dehydration and serpentinization processes. For the relocated seismicity distribution, clusters of events align perpendicular to the trench, and crustal seismicity is also evidenced, along with earthquakes located close to the trench axis. We also compute Regional Moment Tensors to analyze the different sources of seismicity after the mainshock. Aside from thrust events related to the subduction process, normal and strike-slip mechanisms are detected. We suggest that the presence of subducting seamounts coming from the Carnegie Ridge act as erosional agents, helping to create a scenario which promotes locking and allows seismicity to extend up to the trench, along zones of weakness activated after large earthquakes.

1. Introduction

The South American subduction zone has a long history of large megathrust earthquakes and in the past decades a variety of different types of seismicity have been identified, including repeating earthquakes, seismic swarms and slow slip events. During the last century, the Ecuadorian-Colombian margin has experienced several major earthquakes (Ramirez, 1968; Kelleher, 1972; Abe, 1979; Herd et al., 1981; Kanamori and McNally, 1982; Mendoza and Dewey, 1984; Beck and Ruff, 1984; Sennson and Beck, 1996). More recently, slow slip

^{*} Corresponding author at: Geophysical Institute, Karlsruhe Institute of Technology, Hertzstr. 16, Geb.6.42, 76187, Karlsruhe, Germany. E-mail address: sergio.leon-rios@kit.edu (S. León-Ríos).

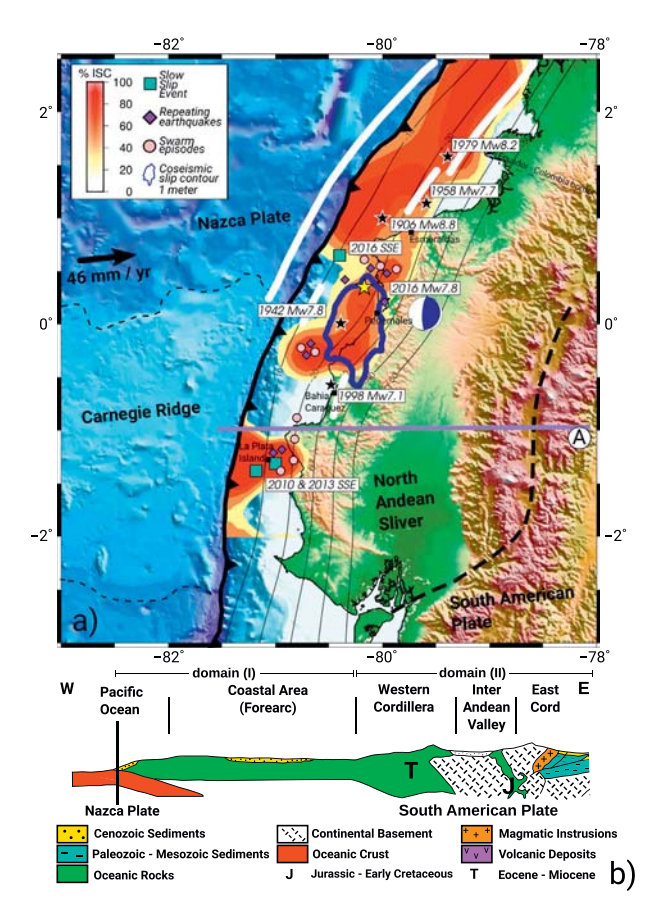


Fig. 1. (a) Seismotectonic characteristics of the central coastal segment of the Ecuadorian margin. Inland and seafloor topography was derived by Michaud et al. (2006). Segmented line shows the Dolores-Guayaquil Megashear that creates the North Andean Sliver. Bold arrow shows the convergence rate between the Nazca plate and the North Andean Sliver (ref). Black stars and white solid lines represent the epicenters and estimated ruptures of the last large subduction earthquakes occurred along the margin since 1906. Squares, diamonds and circles are showing the Slow Slip Events, repeating earthquakes and swarms sequence, respectively, reported by Rolandone et al. (2018). Interseismic coupling derived by Nocquet et al. (2017) and Rolandone et al. (2018) is showed in background. Yellow star is showing the epicenter of the 2016 Mw 7.8 Pedernales earthquake. Focal mechanism and coseismic slip contour, in blue solid line, were obtained by Nocquet et al. (2017). Trench data from Collot et al. (2004). Purple solid line shows the location of the profile in panel b. (b) Structural sketch of the Ecuadorian margin showing the main morphological structures. Figure edited from Jalliard et al. (2000). (For interpretation of the references to color in this figure legend, the reader is referred to the web version of this article.)

events have been observed (Mothes et al., 2013; Vallée et al., 2013; Chlieh et al., 2014; Segovia et al., 2015; Vaca et al., 2018; Collot et al., 2017; Rolandone et al., 2018), in addition to seismic swarms (Segovia, 2001; Segovia et al., 2009; Vaca et al., 2009) and repeating earthquakes (Rolandone et al., 2018) (Fig. 1).

In 1906 a megathrust earthquake Ms 8.7 (Kelleher, 1972), re-estimated to Mw 8.8 (Kanamori and McNally, 1982) and more recently to Mw 8.4 (Yoshimoto et al., 2017), ruptured the subduction segment along central and northern Ecuador and southern Colombia generating severe destruction which reached up to 100 km inland. The rupture extent of this earthquake is still under discussion. Whilst Kanamori and McNally (1982) suggested a rupture of approximately 500 km length, Yoshimoto et al. (2017) proposed a smaller rupture area mainly located near the trench. The 1906 earthquake also caused permanent coastal uplift and generated a destructive tsunami (Ramirez, 1968; Kelleher, 1972; Abe, 1979; Herd et al., 1981; Kanamori and McNally, 1982).

Subsequently, smaller earthquakes of diverse magnitudes (between Mw 7.0 to Mw 8.2) ruptured with thrust mechanisms, leading to several authors proposing a segmentation of the subduction zone along the northern Ecuadorian margin (i.e. Marcaillou et al., 2006; Gailler et al., 2007). In 1942, a Mw 7.8 earthquake occurred close to the coastal city of Pedernales affecting an area of ${\sim}200\,\mathrm{km}$ x ${\sim}90\,\mathrm{km}$. The epicenter was located at the southern edge of the rupture region, suggesting that the event propagated to the NE (Kelleher, 1972; Sennson and Beck, 1996). In 1958, the Mw 7.7 Colombia-Ecuador earthquake (Kanamori and McNally, 1982) broke a small segment of the 1906 megathrust earthquake in the offshore portion of the Esmeraldas province to the North. Like the 1942 earthquake, the 1958 event showed a rupture propagation in the NE direction (Rothé, 1969; Kelleher, 1972; Mendoza and Dewey, 1984). Finally, in 1979, the largest event of this series of major earthquakes occurred close to the Ecuadorian-Colombian border with magnitude of Mw 8.2 also rupturing in a NE direction along ~230 km of the margin (Herd et al., 1981; Kanamori and Given, 1981: Beck and Ruff, 1984).

Between the equator and south of the Carnegie Ridge (CR), there have been few large subduction earthquakes recorded (Egred, 1968; Dorbath et al., 1990; Bilek, 2010) with only two events of Mw > 7.0 (in 1956 and 1998) occurring close to Bahia Caraquez (Storchak et al., 2013). However, a high rate of seismicity up to Mw 6.5 has been registered in this region (Vallée et al., 2013) suggesting that the accumulated stresses are released by different mechanisms than in the northern segment (White et al., 2003; Agurto-Detzel et al., 2019). Moreover, the area shows a complex slip behavior, with different types of seismic activity highlighted in Fig. 1.

The Mw 7.8 Pedernales earthquake occurred in 2016 and led to the largest earthquake-related loss of life (668, Lanning et al., 2016) in Ecuador since the 1987, Mw 7.1 Salado-Reventador event, which occurred in the Andean volcanic arc that killed around 1000 people (Bolton, 1991; Beauval et al., 2010). The 2016 earthquake also affected the Ecuadorian economy due to widespread destruction of houses, hotels and hospitals (Lanning et al., 2016). One month after the earthquake, a dense temporary network (10-30 km station spacing) was deployed in collaboration with the Instituto Geofisico de la Escuela Politecnica Nacional (IGEPN) and several international institutions covering the rupture area. Instrumentation included Ocean Bottom Seismometers (OBS), inland short period and broadband sensors, which complemented the stations of the permanent Ecuadorian seismic network (Alvarado et al., 2018). The combined array recorded the unfolding aftershock sequence up to one year after the mainshock. Although large subduction thrust earthquakes are well documented historically, occurring extensively throughout the entire South American margin, it is only over the last decade that dense monitoring seismic networks have been deployed to record the aftershock sequences of such events. This allows for highly accurate hypocentral relocations enabling detailed investigations into the physical processes occurring within the rupture zone.

One of the major limitations in imaging the seismicity distribution along the Ecuadorian margin is the lack of a robust and well constrained velocity model for the area. The unprecedented seismic coverage provided by the international aftershock deployment offers a unique opportunity to better resolve the velocity structure of this region with the Pedernales earthquake sequence. The recorded data will improve our knowledge of the seismotectonic structures, such as the CR and the Atacames seamounts, along with understanding the mechanisms that control subduction processes in the area.

Although the Ecuadorian margin has been widely studied, there is still no consensus on a representative one-dimensional (1D) velocity model. An improved 1D regional model together with well-located aftershocks recorded by our dense seismic monitoring network will provide better constrained seismic velocities in the area and, the foundation and starting model for future detailed 3D seismic imaging.

Currently, the available velocity models for the Ecuadorian margin

are usually focused in small areas or have limited resolution due to the lack of instruments monitoring the offshore and coastal portion of the country; they are also affected by along strike heterogeneities observed in the region. At present, the national network of seismographs of the geophysical institute (RENSIG) from IGEPN uses a five-layer model (called ASW; for detailed values see Font et al. (2013)) and is used by the IGEPN for locating tectonic events in Ecuador. It, therefore, results in large errors in hypocenter location, especially regarding depth of subduction related seismicity (See Supplementary Material 1). Font et al. (2013) built an a-priori three-dimensional P-wave velocity model for the Ecuadorian subduction margin (4° N - 6° S, 83° W - 77° W), obtained via a joint compilation of marine seismics, gravimetric data, geological observations and seismicity of the region. The model is an improvement for the forearc and provides better hypocentral solutions for the coastal area but has limited capabilities due to the absence of an S-wave velocity model. Gailler et al. (2007) inverted wide-angle seismic data to describe deep structures present offshore of the Ecuadorian -Colombian border. In the same area, Agudelo et al. (2009) also improved the structural model using a combined data set of multichannel seismic reflection and wide-angle data. Cano et al. (2014) provide a 3D velocity model encompassing the rupture of the 1958 earthquake. Both models provide insights about offshore velocities. Further to the south of our study area, Calahorrano et al. (2008) developed a velocity model using marine seismic experiments representing the area close to the Gulf of Guayaquil. However, all three models are located outside of the Pedernales rupture area and outside the area covered by our temporary seismic array. Finally, Graindorge et al. (2004) analyzed the velocity structure in the Carnegie Ridge (CR) area using onshore and offshore wide-angle data to calculate a two-dimensional model. Although our array covers a portion of the CR, this model is not appropriate for the whole area covered by the array due to the anomalous structure of this bathymetric feature.

Using high quality manually picked arrival times (P and S), we develop a minimum 1D velocity model for P- and S-wave velocities of the area affected by the Pedernales earthquake and post-seismic sequence. Based on a Monte Carlo-like approach in which we use a set of 5000 randomly perturbed velocity models as starting models for our inversion, we obtain a new robust minimum 1D velocity model for our study area. Finally, we analyze in detail the seismicity recorded offshore Bahia Caraquez, close to the trench, by determining Regional Moment Tensors (RMTs) to explore the correlation between the distribution of the events, the seismogenic contact and possible faults that might be re/activated due to the mainshock.

2. Seismo-tectonic setting of the Pedernales earthquake

2.1. Structural setting

The Ecuadorian margin is dominated by a convergent regime that involves the subducting oceanic Nazca plate and the overriding continental South American plate. This process occurs with a relative convergence rate of 55 mm/yr (Kendrick et al., 2003) in the N80°E direction. The margin is highly segmented and mainly of erosional type (Collot et al., 2002; Gailler et al., 2007; Marcaillou et al., 2016) creating diverse patterns in seismicity in the subducting and overriding plates as well as along the plate interface. Broadly, the Ecuadorian territory (1°N - 3°S) can be divided into three main domains extending inland from the margin (Jaillard et al., 2000) and our study area comprises mainly along domain (I) and part of domain (II). The profile A, in Fig. 1b, shows the marine forearc including a small layer of sediments of 500 m to 1000 m thick. The coastal region is characterized by the presence of bathymetric features such as the aseismic CR. The CR (~280 km wide and 2 km high) is located near the Ecuadorian trench between latitude 0° and 2°S (see Fig. 1a). The CR was formed by the Galapagos hot-spot located about 1000 km west of the coastline of Ecuador and is currently subducting in an ENE direction. The marine forearc has a series of seamounts such as the Atacames chain which subduct beneath the South American plate and is inferred to play an important role in the nucleation of large subduction earthquakes (Marcaillou et al., 2016). The coastal region shows accreted oceanic terranes from the late Cretaceous-Paleogene period. The width of this domain (I) varies longitudinally from 50 to 180 km, has low relief with < 300 m altitude, and is filled with sediments from the Andes, creating several alluvial basins. The second domain (II) is the Andean chain that involves the Western cordillera, with deformed rocks from accreted oceanic crust, and the Eastern cordillera (Cordillera Real) which contains metamorphic rocks from the Paleozoic to Mesozoic (Litherland, 1994). Both areas are separated with Tertiary to Quaternary volcanic and volcanoclastic rocks that were deposited in the Interandean Valley. At ~3°S, the Chingual-Cosanga-Pallatanga-Puna (CCPP) fault zone separates the continental plate in two (Alvarado et al., 2016), extending throughout the Puna segment, through the Colombian border and towards Venezuela, creating the North Andean Sliver (NAS) shown in Fig. 1. In front of the NAS, the Nazca Plate is < 26 Ma old (Lonsdale, 2005) and subducts at a relative rate of about 46 mm/yr (Chlieh et al., 2014). More specifically, if we consider the coseismic slip derived by Nocquet et al. (2017) and the aftershock activity analyzed by Agurto-Detzel et al. (2019), the area affected by the Pedernales earthquake extends from Esmeraldas canyon in the north (\sim 1.5°N), down to La Plata area in the south (\sim 1°S). In this segment, the depth of the trench varies from 3.7 km in the north to 2.8 km at the crest of the CR (Collot et al., 2004) in the south. Moreover, the oceanic crust thickness shows an along strike variation from 5 km in the north to 14 km in the south, reaching its maximum of 19 km beneath the crest of the CR (Meissnar et al., 1976; Calahorrano, 2001; Sallarès and Charvis, 2003; Sallarès et al., 2005; Graindorge et al., 2004; Garcia Cano et al., 2014).

2.2. The Pedernales earthquake and its aftershocks

On April 16th, 2016, the Mw 7.8 Pedernales earthquake occurred in the central coast of Ecuador, close to the city of Pedernales. This estimated event focal depth is 20 km (Nocquet et al., 2017) and the rupture is characterized as a thrusting mechanism consistent with the megathrust on the plate interface. The Pedernales earthquake ruptured an estimated area of 100 km × 40 km (Nocquet et al., 2017) and propagated along strike from north to south. Although there are different rupture areas proposed for the 1906 earthquake (e.g. Kanamori and McNally, 1982; Yoshimoto et al., 2017), the edges of the 2016 mainshock appear to coincide with the southern boundaries of the 1906 earthquake. This segment of the subduction zone last ruptured in a Mw 7.8 earthquake in 1942. At the southern limit, the rupture coincides with the northern edge of the 1998 Mw 7.1 earthquake in Bahia Caraquez. The Pedernales earthquake affected an area where large megathrust earthquakes, with magnitudes > 7, occurred in the past. Its occurrence correlates with a locked area of interseismic coupling (Chlieh et al., 2014; see Fig. 1).

3. Network and data processing

3.1. The seismic aftershock network

Immediately after the 2016 Pedernales mainshock, an international collaboration of several institutions including; IGEPN from Ecuador, the French Centre d'études et d'expertise sur les risques, l'environnement, la mobilité et l'aménagement (CEREMA) and GEOAZUR institutes, Lehigh University and University of Arizona from the United States and the University of Liverpool from the United Kingdom, coordinated a rapid response effort to deploy a temporary seismic array. One month after the Pedernales earthquake, we deployed a dense temporary seismological array of broadband and short period seismic stations equally distributed inland along the area affected by the aftershocks (Meltzer et al., 2019). Ocean Bottom Seismometers (OBS) were installed along

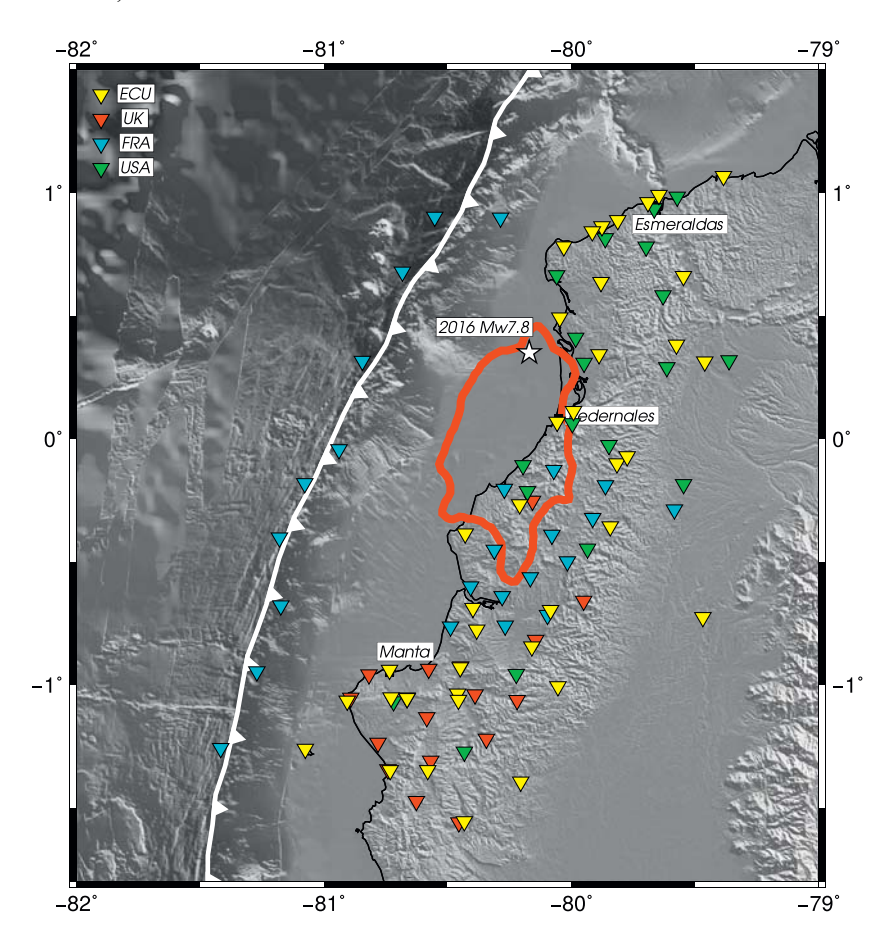


Fig. 2. Seismic aftershock deployment. Inverted triangles represent the stations installed along the Ecuadorian margin. Yellow: backbone network including CMG-3ESP, Trillium compact, Trillium 120p, L4C, TSM-1 Strong Motion operated by the Instituto Geofisico de la Escuela Politecnica Nacional de Ecuador (IGEPN). Red: Broadband Trillium compact and short period Lennartz LE3D Lite instrumentation from the University of Liverpool, United Kingdom. Blue: intermediate period CMG-40T and Ocean Bottom Seismometers from GeoAzur, France. Green: Broadband Guralp CMG-3T and STS-2 from IRIS PASSCAL deployed by the University of Arizona and Lehigh University, United States. Most of the instruments deployed on site were recording at 100 Hz. White star is showing the epicenter of the 2016 Mw 7.8 Pedernales earthquake. Coseismic slip contour in red solid line was derived by Nocquet et al. (2017). Inland and seafloor topography was derived by Michaud et al. (2006). Trench data obtained from Collot et al. (2004). (For interpretation of the references to color in this figure legend, the reader is referred to the web version of this article.)

the trench to complement the stations deployed on land. Fig. 2 shows the spatial distribution of the full array including both temporary and permanent stations consisting of > 80 stations with a station spacing of approximately 10–30 km. The RENSIG Ecuadorian network is a mix of diverse instrumentation including CMG-3ESP, Trillium compact, Trillium 120p, L4C, TSM-1 Strong Motion instruments. The temporary array consists of: (i) short period Lennartz LE 3D Lite recording at 100 Hz; (iii) intermediate period seismometers CMG-40T recording at 200 Hz; (iii) broadband stations Trillium Compact, Guralp CMG-3T and STS-2 recording at 100 Hz. The temporary array was fully operative from May 2016 to June 2017. OBSs were recording between mid-May to November in 2016, at 100 Hz.

3.2. Data processing

3.2.1. Onset detection

Based on the initial catalogue provided by IGEPN (http://www. igepn.edu.ec/solicitud-de-datos) with 1677 reported seismic events between May 15th and August 26th, 2016, we created a high quality dataset to be used for the 1D inversion process. We first selected aftershocks with local magnitude (M_L) > 3.5 located in the vicinity of the temporary array. From this catalogue, P- and S-wave arrival times were manually picked for 345 aftershocks using the Seismic Data Explorer (SDX) software package (http://doree.esc.liv.ac.uk:8080/sdx). The events were located based on an average 1D velocity model derived from Font et al. (2013); SDX utilizes a modified hypo71 algorithm for hypocenter location (Lee and Lahr, 1972). Following the procedures from Agurto et al. (2012) and Hicks et al. (2014), we assigned pick error categories, referred as weights, from 0 to 4 to describe the quality of the selected arrival times. Each weight corresponds to the following time uncertainties: Weight 0 (< 0.04 s); Weight 1 (0.04-0.1 s); Weight 2 (0.1-0.2 s); Weight 3 (0.2-1 s); Weight 4 (> 1 s).

3.2.2. Minimum 1D model

From the manually picked catalogue, we further filter to ensure only the highest quality events remain for the minimum 1D velocity model inversion using VELEST (Kissling et al., 1994). We selected earthquakes with at least 10 P- and 10 S-onset observations and an azimuthal gap $< 200^\circ$. In total we obtained a dataset of 227 events with an average of 21 and 17 P- and S-onset times respectively, which contains 4939 P-phases and 3931 S-phases (See Supplementary Material 2).

To minimize the influence of strong topography changes and avoid bias due to the depth of the OBSs, we followed the strategy described by Husen et al. (1999) and Hicks et al. (2014) and set station elevation equal to zero. Station correction terms therefore account for both, the relative elevation and the site-specific velocity differences. Station correction terms were strongly damped (damping = 1000) during the Vp inversion, allowing for greater initial exploration of the Vp parameter space. For the Vs inversion, the damping was decreased (damping = 20), this allows the station-delay terms to absorb errors due to the velocity fluctuations near the stations.

We selected five starting models (see Supplementary Material 3) to cover a wide range of plausible cases: (1) the average model derived from Font et al. (2013), selected as it covers our entire study area with a 3D regional model, (2) an average offshore model based on previous studies by Gailler et al. (2007) and Agudelo et al. (2009), and (3–5) modified versions of the ASW model, used by IGEPN (Font et al., 2013). For models 3–5, we vary the Moho depth between the range of 40 and 60 km. To cover the entire range of feasible velocity models, we created 1000 random variations of each reference velocity model, sampling from a uniform distribution with bounds \pm 0.5 km/s of the reference model velocity. We, therefore, explore 5000 starting models in total, derived from the five classes of models. From the 5000 starting models, the P-wave velocity model with the lowest overall misfit to the travel time picks (RMS 0.335 s) is assumed as our best Vp representation. The

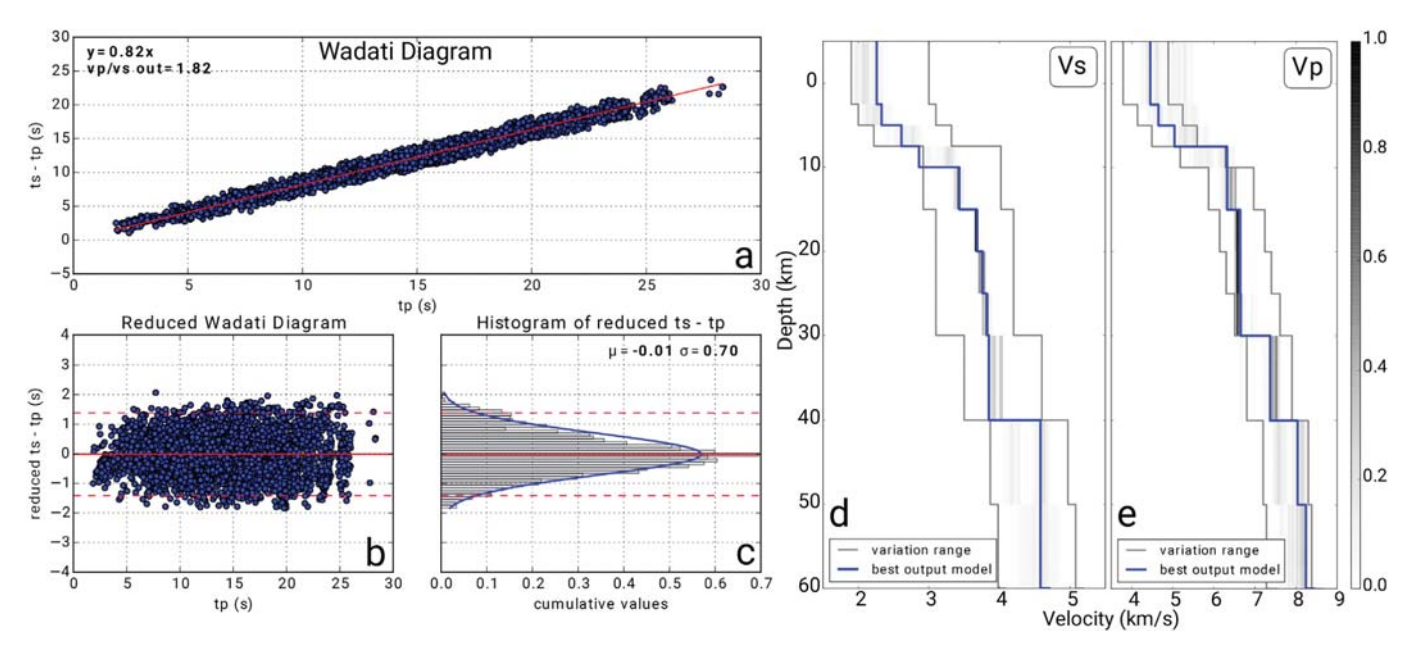


Fig. 3. (a) Wadati Diagram (Wadati and Oki, 1933) used to compute the observed Vp/Vs ratio using all the available onsets. Red line shows the linear fit for the data which indicates a Vp/Vs ratio of 1.82. (b) Reduced Wadati Diagram used to remove outliers from onset times picked. |Vp/Vs| > 2 was used as a cutoff value. Solid red line: y = 0. Segmented red l

density plots in Fig. 3d and e demonstrate how the best 200 solutions for the inverted Vp and Vs models have a clear convergence towards the best solution between 7.5 km and 40 km depth. The shallowest layers (down to 7.5 km) do also exhibit a convergence towards a minimum velocity solution, however, due to a lack of events occurring in this region, the solution shows a slightly wider range of possible velocities. For the deeper layers (> 40 km), absolute velocities cannot be constrained due to the lack of data and therefore several cluster of solutions can be observed. To detect picking outliers and to estimate an average Vp/Vs ratio for the region, we performed Wadati analysis (Wadati and Oki, 1933), displayed in Fig. 3a. Onset times show a clear trend for (ts tp) as a function of tp, a linear trend fit provides a Vp/Vs ratio value of 1.82. A reduced Wadati diagram was also used to have a better control on the outliers in our dataset. Onsets greater than 2σ from the Vp/Vs trend were removed (see Fig. 3b). The final dataset of arrival times is represented in a histogram in Fig. 3c with a mean of ts-tp of 0.01 s and a variance of $0.70 \,\mathrm{s}^2$.

Finally, using our best Vp model and the Vp/Vs ratio (1.82) obtained via Wadati analysis, we built an initial 1D S-wave velocity model. The inversion for the optimum S-wave velocity model follows the same procedure as for the P-wave velocity model. We perturbed the S-wave velocities of the starting model within a range of \pm 0.5 km/s, creating 1000 models where both P- and S-phases were simultaneously inverted for. In this step, we fixed the Vp velocities to avoid changes in the previously obtained Vp model by S-wave observations. The solution with the lowest RMS (0.303 s) was accepted as our final S-wave model along with the final set of station corrections and hypocentral locations. By using a Monte Carlo approach for selecting the starting model, we mitigate the dependency of the final model from starting model as we sample a much larger model space.

3.2.3. Regional moment tensors

A significant portion of the aftershocks are related to the megathrust faulting displaying reverse solutions consistent with the slip of the plate interface (Agurto-Detzel et al., 2019). We focus our RMT analysis on the seismicity recorded throughout offshore Bahia Caraquez and Cabo

Pasado which exhibits various faulting mechanisms. In this area, we observe events distributed close to the trench (5 km-10 km), however, due to the trade-off between hypocentral depth and origin time, depth location uncertainties in this region are larger than the average. These events could, therefore, be located at the interface, in the upper or in the downgoing plate. To better constrain the focal depth parameter for events in this region, we calculated RMT solutions for 14 events by performing a full waveform inversion using the isola package (Sokos and Zahradník, 2008, 2013). We analyzed events reported by IGEPN with local magnitude (M_L) > 4.0. The location was fixed to the epicentral locations obtained from our relocation process with VELEST, and the depth is allowed to vary. Green's functions are calculated from a simplified version of our minimum 1D model where the shallowest 8 layers are merged into 4 layers (see Supplementary Material 4). Seismic records were bandpass filtered between 0.04 and 0.09 Hz before the inversion, and between 4 and 10 broadband stations were used for the inversion process of each event.

4. Results

Our final minimum 1D model, represented by 12 layers, with P- and S-wave velocities and the Vp/Vs ratio are given in Table 1 and shown in Fig. 4. The model is well constrained between 7.5 km and 40 km, where most of the seismicity is concentrated (see Fig. 4). Although, most of the ray paths are concentrated in the shallower layers, we observe some rays down to 40 km depth, which help us to constrain the average of the oceanic and continental Moho depth. At shallower depths, the lack of crustal events ($< 7.5 \, \text{km}$ depth) means we are not able to obtain reliable absolute velocities due to the trade-off with station corrections; at greater depths ($30 \, \text{km}$ – $40 \, \text{km}$) the ray path distribution still shows rays passing through, however at depths $> 40 \, \text{km}$ the limited extend does not allow a robust estimation of the average velocities.

The obtained model shows a Vp that fluctuates between 4.45 km/s and 5.04 km/s, in the top layers (down to 7.5 km). From 7.5 km depth to 25 km, Vp consistently increases from 6.3 km/s to 6.6 km/s. Between 30 km and 40 km the constant increase of Vp (from 7.37 km/s at 30 km

Table 1
Minimum 1D model. Absolute velocities and Vp/Vs ratio are listed in terms of depth.

Depth (km)	Vp (km/s)	Vs (km/s)	Vp/Vs
-5.00	4.45	2.26	1.97
2.50	4.65	2.32	2.00
5.00	5.04	2.59	1.95
7.50	6.32	2.90	2.18
10.00	6.32	3.42	1.85
15.00	6.64	3.69	1.80
20.00	6.64	3.76	1.77
25.00	6.65	3.80	1.75
30.00	7.37	3.81	1.93
40.00	8.04	4.64	1.73
50.00	8.24	4.64	1.78
60.00	8.45	4.71	1.79

to $8.04\,\mathrm{km/s}$ at $40\,\mathrm{km}$) suggests an area of transition from crust to mantle. At $40\,\mathrm{km}$ Vp reaches $8.04\,\mathrm{km/s}$, which can be related with continental upper mantle velocities. Finally, the absence of data between $40\,\mathrm{km}$ and $60\,\mathrm{km}$ depth, does not allow us to resolve the P-wave velocity, so the resulting values are mainly influenced by our reference model derived by Font et al. (2013) (see Fig. 4).

Vp/Vs ratio shows a weighted arithmetic mean of 1.82 for the whole model. In the top layers (down to 7.5 km depth) we find a high Vp/Vs ratio that varies from 1.97 to 2.18. At 10 km depth, the Vp/Vs ratio decreases to 1.85 down to 30 km depth where it rises to 1.93. The Vp/Vs ratio is not well resolved at depths > 40 km as we do not have enough data to constrain that area (see Fig. 4).

Statistics for the inversion also show the robustness of our model. Arrival time residuals were classified according to the weights described in the previous section. Histogram plots in Fig. 5 indicate that most of the P- (99%) and S- (88%) phase picks are classified between weights 0 and 1. For high quality P-wave onsets (weight 0 and 1), the standard deviations of residuals is $0.24\,\mathrm{s}$ and $0.26\,\mathrm{s}$, respectively. For the S phase, the deviation varies from $0.48\,\mathrm{s}$, for weight 0, to $0.52\,\mathrm{s}$ for weight 1. Observations for each station display residuals with a normal distribution concentrated between -1 and $1\,\mathrm{s}$ (See Supplementary Material 5). Overall, the obtained catalogue has a variance of $0.084\,\mathrm{s}^2$, which is above the variance based on the accuracy provided by the

manual picking of $0.027\,\mathrm{s}^2$ indicating that we are not overfitting our onset time data.

Our new minimum 1D-velocity model was then used to relocate the 227 manually-picked events (See Supplementary Material 6 for comparison with the original locations). To test the accuracy of the resulting hypocenters, we performed a stability test by randomly perturbing hypocenters starting locations by between 7.5 km and 12.5 km in latitude, longitude and depth. We then relocated the events using our minimum 1-D velocity model and station corrections. The location of the recovered seismicity shifts only marginally respect to the original positions, leading to an estimation of the relocation uncertainties around 1 km in latitude and longitude, and 2.7 km in depth (See Supplementary Material 7). Overall, the relocated seismicity displays an average error of 1.38 km and 1.57 km for the horizontal and vertical component, respectively. As hypocentral uncertainty is shown to increase with distance offshore, we separately calculate the location errors for the offshore seismicity. For this data subset, we obtain average uncertainties of 1.53 km for the horizontal axis and 2.15 km for the vertical axis.

The relocated aftershocks are shown in Fig. 6. The seismicity is distributed between 5–10 km and 100 km eastward of the trench and between 2 km and 35 km in depth. The most important features are as follows:

- (1) We observe that our epicentral distribution for the analyzed aftershocks are in agreement with other related studies (e.g. Meltzer et al. (2019), Agurto-Detzel et al. (2019)). We find that events with local magnitude > 3.5 are generally distributed outside the coseismic slip area of the 2016 Pedernales mainshock and skew towards the trench.
- (2) Most of the seismicity along profiles AA' and BB' is located along the plate interface. Slab1.0 (Hayes et al., 2012) is used as a reference in Fig. 6, however a comparison between both Slab1.0 (Hayes et al., 2012) and Slab2.0 (Hayes et al., 2018) is shown in Supplementary Material 8. The northern profile AA' demonstrates the differences between the interface for both models, in the region, Slab2.0 is relatively deeper than the Slab1.0 interface; the located aftershocks are distributed between both Slab1.0 and Slab2.0. These relative changes in extensively used slab models further highlight the complexities the Ecuadorian margin along strike.

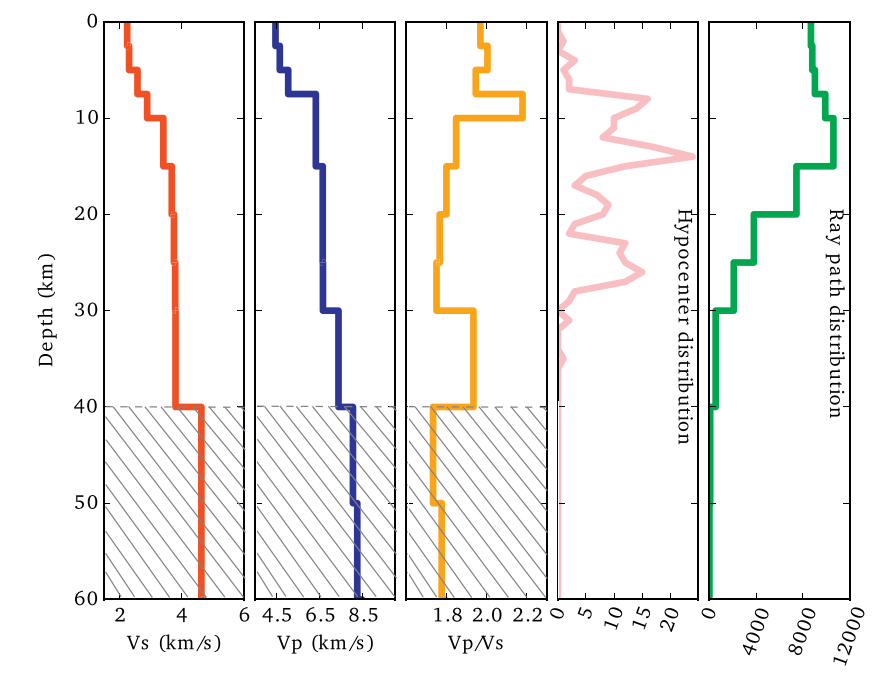


Fig. 4. Final 1D velocity model showing the absolute Vp (solid blue line) and Vs (solid red line) velocities, Vp/Vs ratio (solid orange line) and a histogram of the seismicity distribution with depth. Dashed area indicates the area where our minimum 1D model is unconstrained. Velocity values for depths > 40 km were derived by Font et al. (2013) and were included in our initial reference model. (For interpretation of the references to color in this figure legend, the reader is referred to the web version of this article.)

Normalized Histogram Residuals classified by quality of picks

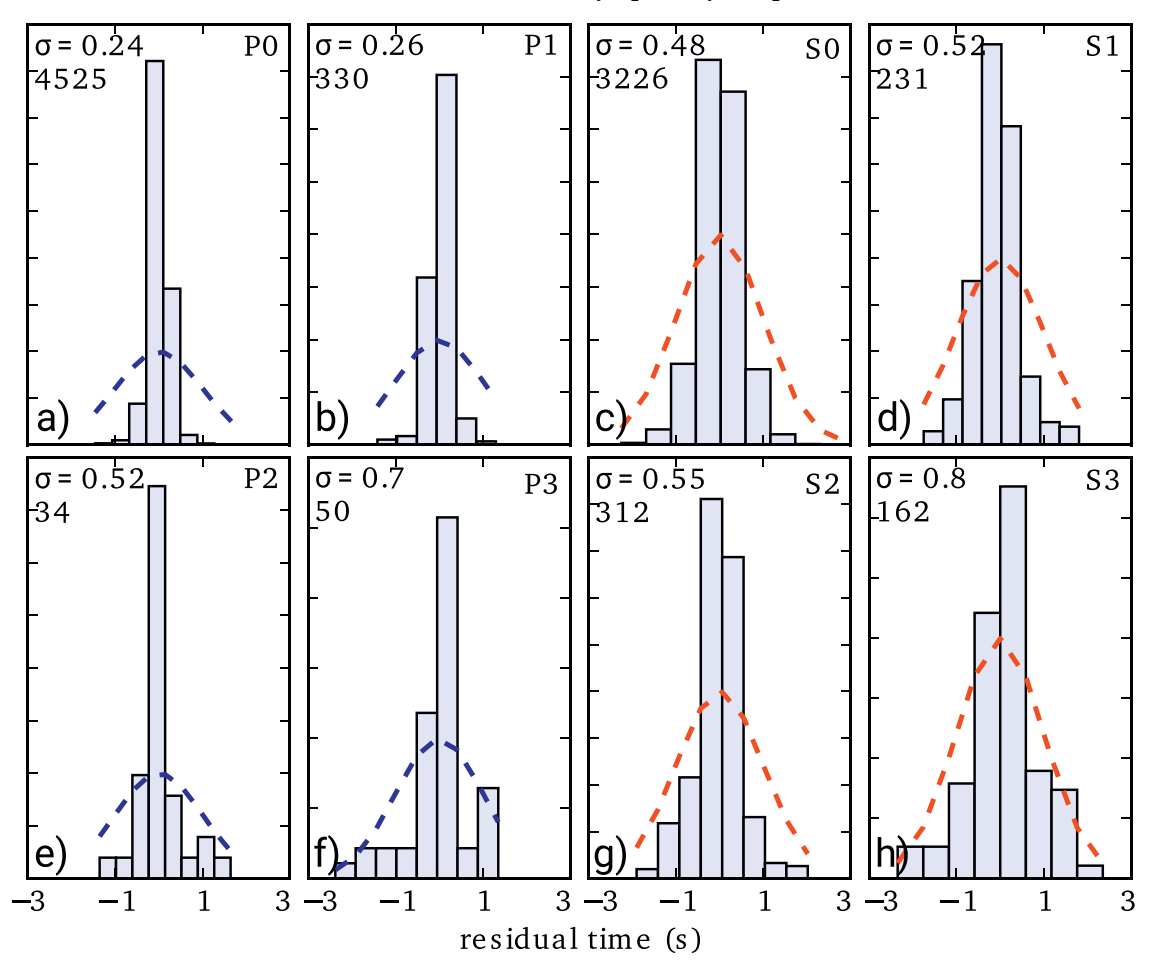


Fig. 5. Histograms for the residuals obtained after the inversion of both Vp and Vs velocities. Plots were classified according to the quality of picks indicated in the top right corner. Each weight corresponds to the following time uncertainties: Weight 0 < 0.04 s); Weight 1 (0.04-0.1 s); Weight 2 (0.1-0.2 s); Weight 3 (0.2-1 s); Weight 4 > 1 s). Segmented blue and red lines represent the fit of the data. Standard deviation and number of observation are displayed on the top left corner of each plot. (For interpretation of the references to color in this figure legend, the reader is referred to the web version of this article.)

- (3) Clustered activity in the overriding plate can be observed in both northern (AA') and southern (BB') profiles.
- (4) Profiles AA' and BB' (see Fig. 6) show that a portion of the aftershocks reach the trench. This has been demonstrated as a robust feature due to specific bias testing of the offshore relocated seismicity.

Although, the formal locations errors stated before are < 3 km in depth, absolute locations errors can be significantly larger. To identify whether the events distributed close to the trench are located in the subducting or the overriding plate, we calculated RMT solutions to better constrain the hypocenter depth. We focus here on the offshore seismicity located close to profile BB' and calculated 14 RMTs. This is an area where Agurto-Detzel et al. (2019) reported a single anomalous strike-slip event at about 10 km depth. Fig. 6 shows the solutions superimposed over the relocated aftershock activity. Additional information about the waveform inversion fit and comparison with other MT catalogues are shown in Supplementary Material 9, 10 and 11. We also compare the difference between depths obtained from the velocity model inversion and isola. Events with depths between 5 km and 15 km, based on arrival times, show a small difference in their depth locations in comparison to the RMT solutions. For the offshore seismicity located with depths > 15 km using travel times, the RMT centroid depths are

shallower than those of the hypocenters (see Table 2 and Supplementary Materials 12 and 13).

The majority of the aftershock RMTs for the Pedernales segment exhibit a thrust mechanism related to the subduction interface (e.g. Agurto-Detzel et al., 2019). However, we also find events that display extensional and strike slip faulting mechanisms, distributed along the marine forearc. Table 2 summarizes our results listing the centroid information, nodal planes, magnitude, variance reduction and double-couple percentage.

5. Discussion

5.1. Velocity Model

Fig. 4 shows the best 1D velocity model. The histograms show depth distribution of the aftershock seismicity and help to demonstrate the resolution of our model at different depths. Although a more in-depth interpretation requires at least a 2D velocity model, our obtained 1D velocity model allows us to observe and discuss depth ranges and to first order the velocity structure with depth. High Vp/Vs ratio obtained in the shallow layers can be related to hydrated sediments, non-consolidated soils and/or fractured oceanic crust (Peacock, 2001; Hacker et al., 2003a, 2003b; Kato et al., 2010; Pasten-Araya et al., 2018). The

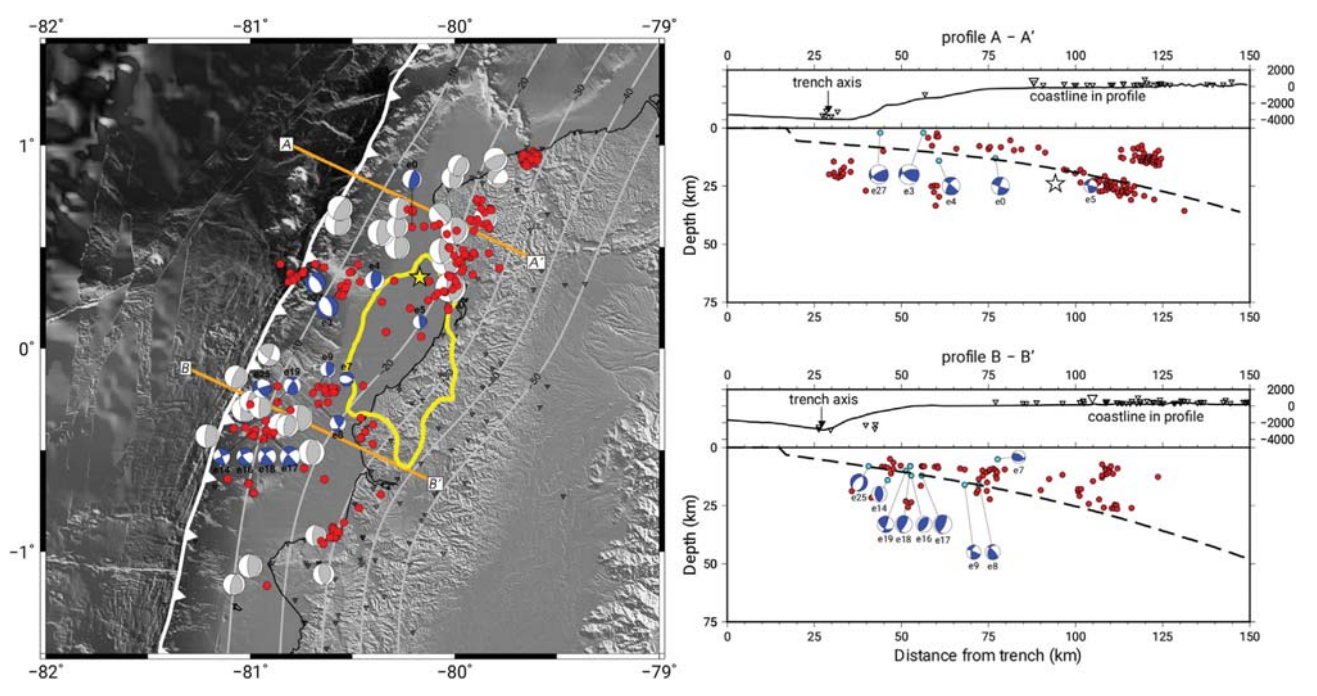


Fig. 6. Mapview and cross sections, 60 km wide, of the relocated seismicity. Red circles indicate the aftershock locations after the inversion with VELEST. Blue beach balls represent the RMT calculated using isola superimposed over the gCMT catalogue in gray. Star shows the location of the 2016 Mw 7.8 Pedernales earthquake. Slab1 from Hayes et al. (2012) is being used as a reference for the in-depth distribution. Inland and seafloor topography from Michaud et al. (2006). Coseismic slip contour derived by Nocquet et al. (2017). Inland and seafloor topography from MMichaud et al. (2006). Trench data obtained from Collot et al. (2004). Slab 1.0 km depth contours from Hayes et al. (2012) are shown in gray lines. (For interpretation of the references to color in this figure legend, the reader is referred to the web version of this article.)

Table 2
Summary of results for the obtained RMT. Depths calculated based on arrival times inversion were included for comparison.

#	Lat (°)	Lon (°)	Centroid depth (km)	Arrival times depth (km)	Strike	Dip	Rake	Mag (Mw)	Var (%)	DC (%)	ID	Date
1	0.6330	-80.2077	13.00	8.24	196	72	94	4.4	80	82.3	e0	2016-06-06 16:45:08
2	0.2940	-80.5730	2.03	4.42	342	<i>57</i>	- <i>79</i>	5.1	68	89.5	e3	2016-06-01 10:05:16
3	0.3740	-80.4910	14.03	11.91	174	60	65	4.4	86	61.2	e4	2016-05-31 15:48:11
4	0.1295	-80.1691	25.03	25.53	173	84	81	3.3	28	63.8	e5	2016-05-30 05:48:56
5	-0.2000	-80.5770	5.00	18.37	290	54	-66	3.3	13	71.1	e7	2016-06-21 04:40:24
6	-0.2718	-80.6639	16.03	12.54	49	49	164	3.7	13	31.5	e8	2016-06-02 00:18:59
7	-0.1880	-80.6652	16.03	18.99	175	74	74	3.5	44	62.5	e9	2016-06-01 02:12:22
8	-0.4079	-80.9864	14.02	8.14	247	88	177	3.8	45	76.0	e14	2016-07-07 17:10:13
9	-0.4444	-80.9390	8.03	29.99	143	74	-27	3.9	18	99.1	e16	2016-07-08 04:41:34
10	-0.4268	-80.8981	12.03	7.88	316	89	24	4.6	66	55.6	e17	2016-07-08 07:03:48
11	-0.4047	-80.9177	12.03	22.99	316	86	29	4.2	61	43.3	e18	2016-07-08 07:35:15
12	-0.2629	-80.8675	10.03	22.35	324	50	28	4.0	<i>57</i>	10.4	e19	2016-07-10 06:44:34
13	-0.1967	-80.9427	8.03	_	250	80	35	4.2	23	70.0	e25	2016-05-05 16:06:40
14	0.3242	-80.6818	2.03	4.16	318	61	-110	4.7	57	65.9	e27	2016-06-01 15:00:51

values in this section (up to 2.2 at 7.5 km depth) may reflect an upward migration of fluids coming from the dehydration of sediments subducting within the Nazca plate. Similar cases have been discussed in other areas such as northern Chile (Husen and Kissling, 2001), New Zealand (Barnes et al., 2010), Sumatra (Collings et al., 2012) and Costa Rica (Bangs et al., 2015). As we are dealing with P- and S- onsets coming from both OBS and inland stations, in the depth range between 10 km and 40 km, the subduction process of the Nazca plate descending beneath the South American plate produces an overlapping of velocities from both plates which do not allow us to address each plate individually in a one-dimensional model. However, there is a constant increase in velocities for both P- and S-wave indicating more consolidated rocks. We also identify another increase in the Vp/Vs ratio (Vp/Vs = 1.90) around 30 km depth. A change in Vp/Vs ratio at ~30 km depth agrees with the findings of Hacker et al. (2003a, 2003b) and Bloch et al. (2018) who associated these characteristics with the dehydration of the subducting oceanic plate. Between 30 km and 40 km it is not possible to observe a sharp contrast. However, due to the rapid increase of Vp we suggest a transitional area where the oceanic Moho could be located. At depths > 40 km, Vp reaches values > 8 km/s that can be associated with velocities of the upper mantle (Gailler et al., 2007; Font et al., 2013; Araujo, 2016).

Station correction terms were also calculated in the inversion. Fig. 8 shows the delays obtained for both P- and S-wave onsets. EC16 was used as a reference station because of its central location along the array and large number of observations (total = 384, P=214, S=170). For the P-delay times, the standard deviation for all stations shows that values are concentrated around 0.50 s. Delays for the S phase show a distribution around 0.85 s. In both cases, the obtained values are coherent within the study region following a west to east change of sign that moves from negative to positive. This change is mainly associated with two factors: (1) The eastward dipping of the subducting Nazca plate that produces large residuals in the inversion as VELEST maps the 2D structure into the station correction terms; (2) the

variations in topography of the area, from around 3000 m below sea level at the trench to 700 m above sea level in the coastal range. If we consider the difference in elevation of the array, a geological interpretation will only be valid for the inland stations as the reference station (EC16) is located in this area, and the delay in the OBS can mainly be explained due to the abrupt changes in topography from sea level to the trench (~4000 m depth).

Taking this into account, the difference in elevation for the inland seismic stations range from sea level for stations installed close to the coast to 688 m for the stations deployed at the base of the coastal range. Station correction terms in Fig. 8, especially for the S-phase, show a NE-SW variation in sign from negative to positive which might be related with changes in the geological conditions of the area. Those changes coincide with the Jama Fault System (JFS) mapped in coastal Ecuador (Reyes and Michaud, 2012) and can be attributed to differences in the properties on both sides of the fault. Along the coast, it is possible to find Cretaceous formations (~89 Ma, Luzieux et al., 2006) with rocks from the oceanic crust that were accreted onto the margin and could explain the negative delay in station terms. To the east side of the JFS, less consolidated formations such as conglomerates, volcanic sediments and alluvial formations from the Miocene, Pliocene and Quaternary, respectively, were mapped (Bristow et al., 1977; Cantalamessa and Di Celma, 2005; Cantalamessa et al., 2007) and can be correlated with the positive delay observed in our inversion. This difference in the geological structures is also consistent with the observation that cities far from the epicenter (> 100 km) suffered severe damage due to site effects such as Portoviejo and Chone where the vertical component of PGA reached up to 1.01 m/s² and 1.72 m/s² (IGEPN, 2016) and the delay terms for the S-phase calculated were 2.08 s and 2.57 s, respectively. The role of the fault system in the seismicity of the Central Coastal Ecuadorian margin will be discussed in detail in the next section.

5.2. Aftershocks distribution

The majority of our relocated events with local magnitude > 3.5 are surrounding the coseismic slip area determined by Nocquet et al. (2017). This type of aftershock distribution concentrated on the updip part of the rupture has been previously observed in other megathrust earthquakes along the South American margin such as the Mw 8.8 Maule 2010 earthquake (Rietbrock et al., 2012) and the Mw 8.2 Iquique earthquake (León-Ríos et al., 2016).

The distribution of our relocated aftershocks along the margin are consistent with the observations from Meltzer et al. (2019), Agurto-Detzel et al. (2019) that show seismicity streaks aligned perpendicular to the trench (see Supplementary Material 14). The seismicity distribution during the interseismic cycle (Font et al., 2013) is similar to the aftershock sequence of the Pedernales earthquake and suggests that this behavior could be a regular feature of the Ecuadorian subduction zone (see Supplementary Material 14).

Cross sections AA' and BB', in Fig. 6, show that the depth distribution of the events is consistent with Slab1.0 from Hayes et al. (2012). While the northern section is in a good agreement with the projection of the slab at distances > 50 km eastward from the trench, the southern profile shows seismicity that could indicate a shallower plate interface (see profile BB' in Supplementary Material 8). The subduction of the CR helps to explain this distribution due to the addition of a more buoyant oceanic crust which causes the raising of the seismogenic interface zone. This has been previously proposed by Collot et al. (2004) and Gailler et al. (2007) using active seismic methods in the forearc region of the Ecuadorian margin.

It is also possible to identify clustered seismicity in both sections, north and south, that are located in the overriding plate. This type of activity might be caused by the activation of crustal faults due to changes in Coulomb stress in the area surrounding the coseismic slip (e.g. Ryder et al., 2012).

As previously mentioned, the aftershock seismicity, located in the northern profile AA', occurs very close to the trench, up to \sim 5 km-10 km, which we confirmed using the OBS stations offshore. Usually, seismicity along subduction margins does not extend up to areas close to the trench axis. Although this phenomena has been previously observed when an accretionary prism is present in the subduction zone, even in a erosional regime it is uncommon to observe seismicity with such proximity to the trench (i.e. 2010 Maule, Chile (Rietbrock et al. (2012); Lange et al. (2012)); 2015 Mw 8.3 Illapel, Chile (Ruiz et al., 2016); 2014 Mw 8.2 Iquique, Chile (León-Ríos et al., 2016); New Zealand (Anderson and Webb, 1994); Japan (Asano et al., 2011)). This activity might be related to (1) intraplate deformation due to the bending of the oceanic crust that can causes seismicity in the subducting slab and/or to (2) the absence of a frontal accretionary prism that allows the locking of the megathrust to extend up to the trench, causing seismicity, even at shallow depths.

Finally, the presence of subducting seamounts acting as erosional agents, helps to create a scenario which might promote locking and allow seismicity to extend up to the trench along zones of weakness activated after large earthquakes.

5.3. Deformation in the marine forearc and upper crust

Previous studies by Agurto-Detzel et al. (2019) and Meltzer et al. (2019) have described the overall deformation caused by the Pedernales earthquake. As we now have developed a robust minimum 1D model for the area affected by the 2016 mainshock and also manually determined high precision onset times, we are able to constrain the hypocentral depths in greater detail. We, therefore, will concentrate our discussion on the offshore area close to Cabo Pasado (see Fig. 7) and analyze the deformation in the marine forearc and upper crust based on the diverse seismicity found in this area. The distribution and mechanisms of the 14 calculated RMTs in this study are superimposed over our event locations in Fig. 6. Thrusting focal mechanisms from the gCMT catalogues (Ekström et al., 2012) are also shown and highlight the diversity of our obtained solutions.

In profile AA' we found two events with extensional components (e3 and e27 in Table 2) occurring in the overriding plate. Our RMT solutions agree with the suggestion by Marcaillou et al. (2016) who proposed that seamounts, part of the Atacames chain, could cause the activation of normal faults in the marine forearc of the overriding plate. Normal faulting in the marine forearc has been previously observed in the South American margin (Ruiz et al., 2014), especially in areas within erosive regime like in central Ecuador, where the overriding plate contains a small accretionary prism and a fractured, eroded and hydrated wedge that is easy to break.

Across profile BB', we observed a clear pattern of strike-slip mechanisms distributed along the marine forearc (near the plate interface) and surrounding the scarps in front of Cabo Pasado. This strike-slip sequence lasted for two days between the 7th and 8th July 2016. Fig. 7 shows in detail the distribution of those events. This type of seismic activity in the area has been previously observed by Vaca (2017, fig. 2.7) close to La Plata island (~1°S).

Reactivation of preexisting normal faults in the upper crust after large megathrust earthquakes has been recently observed in many subduction zone settings (i.e. Farías et al., 2011, Ryder et al., 2012, Asano et al., 2011, Kato et al., 2011, Toda and Tsutsumi, 2013). Although normal fault mechanisms are also detected for the Pedernales aftershock sequence we observe a considerable amount of strike-slip seismicity that might be related to the following possible causes:

(1) The pattern followed by the strike-slip events is consistent with the projection of the crest of the CR derived by Pilger (1984) (see Fig. 7). Around 80 km to the north of the CR, the forearc was affected by the subduction of the Atacames seamounts (Collot et al., 2005; Marcaillou et al., 2016) causing deformation on the margin

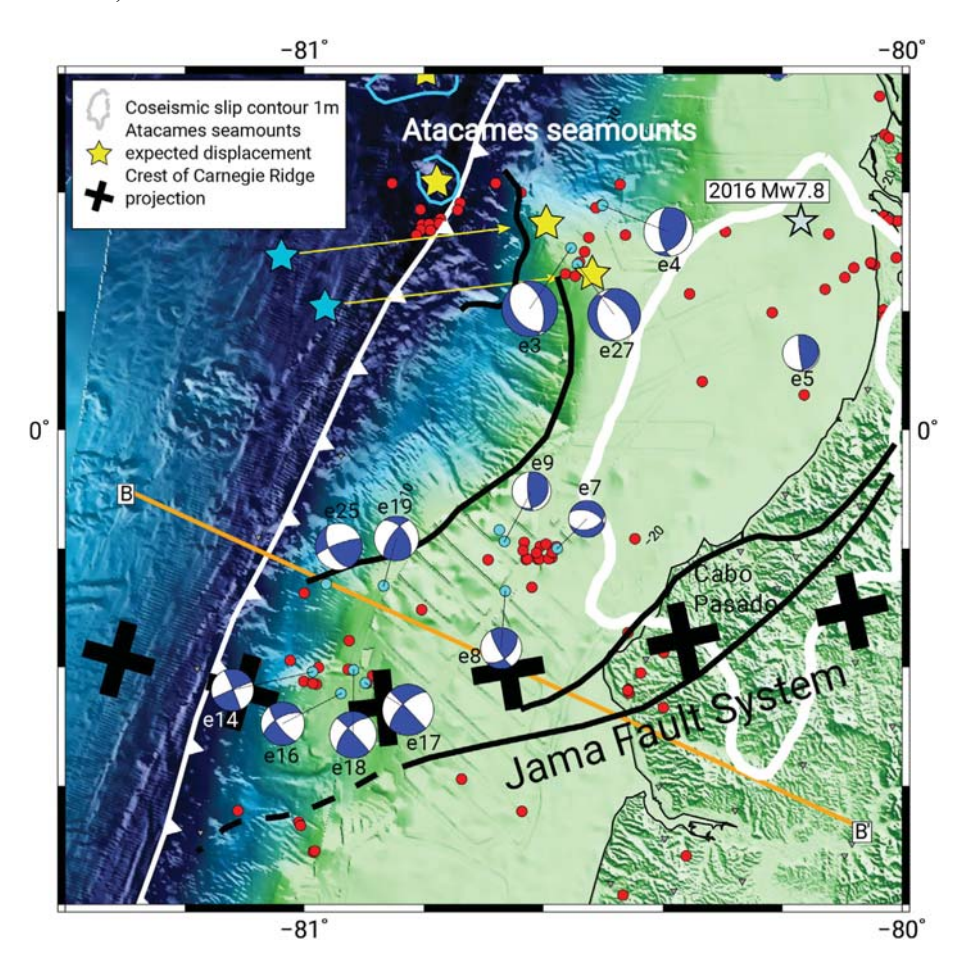


Fig. 7. Zoom into the offshore Cabo Pasado area, where the strike-slip seismicity was detected. Red circles represent the seismicity relocated in the 1D inversion. Blue beach balls are the RMT solutions. Black crosses are the projection of the crest of the CR derived by Collot et al. (2004). Black solid lines show the Jama Fault System and its projection off shore from Collot et al. (2004) and Reyes and Michaud (2012), and the scarps in the marine forearc. Blue and yellow stars are the initial and final position of the Atacames seamounts proposed by Marcaillou et al. (2016). Gray star shows the epicenter of the 2016 Mw 7.8 Pedernales earthquake. Coseismic slip contour derived by Nocquet et al. (2017) is indicated in solid yellow line. Inland and seafloor topography from Michaud et al. (2006). Trench data obtained from Collot et al. (2004). Slab 1.0 km depth contours from Hayes et al. (2012) are shown in gray lines. (For interpretation of the references to color in this figure legend, the reader is referred to the web version of this article.)

and creating two scarps of 25 to 40 km wide separated by a shallow promontory (Collot et al., 2009) (see Fig. 7). This suggests that subduction of the CR beneath the South American plate might create large scale deformation and reactivate transform faulting in the overriding plate.

- (2) The location of the offshore Cabo Pasado seismicity is coincident with a rotational block system proposed by Daly (1989) that extends along the whole Pedernales segment. This system was created 45 Ma ago in the Mid-Late Eocene because of the rapid convergence rate between the Nazca and the South American plates. The interaction of the two convergent plates plus the presence of a major shear fault could have caused faulting in the forearc between the trench and the coast, creating several independent blocks in the Pedernales segment. Rapid changes in the relative velocities of these blocks could have caused both faults and blocks to have been rotated within the bounding shear zones, generating zones of strikeslip faulting at the edges of each block. These features remained inactive after the stabilization of convergence from the Late Miocene (~10 Ma) to the present day. Possible reactivation of the strike-slip faults might be related to the occurrence of large megathrust earthquake.
- (3) Seismicity is associated with the possible extension offshore of the Jama Fault System (JFS) that also coincides with the area where the crest of the CR is located. The JFS could be explained as a large-scale system that was generated to release the stress accumulated by the interaction between the CCPP fault zone and the convergence margin. Collot et al. (2004) proposed the JFS as an active transcurrent fault that extends offshore which was confirmed by Hernández et al. (2011) and Michaud et al. (2015). It is possible that the occurrence of a large megathrust earthquake triggered the nucleation of seismicity along this fault.

In our opinion, a combination between hypothesis (1) and (3) is most likely to explain the observed activity because large-scale strikeslip system as the JFS normally do not extend in one single line but in several strands, covering an entire region as has been observed inland for the same system. In addition, the interaction between the CR and the upper crust where the JFS extends might contribute to the generation of this type of seismicity. These two factors, in addition to a large megathrust earthquake, such as the 2016 Pedernales event, could have provided the conditions to reactivate a strike-slip fault in the marine forearc. This offshore feature might have an important role as a barrier for large megathrust earthquakes by absorbing the stress released during the reverse coseismic and transform it into strike-slip displacement (e.g. Collot et al., 2004).

Whatever the cause is, the occurrence of seismicity associated with the reactivation of a strike-slip fault in the marine forearc is a remarkable observation. Upper crustal activity, related to normal faulting has been often documented: e.g. Pichilemu in central Chile (Farías et al., 2011; Ryder et al., 2012) and also in Japan (Kato et al., 2011). It is therefore interesting to note that strike-slip faults can also be reactivated and should, therefore, be mapped in order to update the hazards map in the region.

6. Conclusions

We inferred a minimum 1D model for the Pedernales segment based on the aftershock sequence ($M_L > 3.5$) of the Mw 7.8 Pedernales earthquake. The velocity structure for both P- and S-phases was obtained after manually picking 345 events recorded by the permanent Ecuadorian seismic network and a temporary array that includes > 70 inland and marine stations installed one month after the mainshock. P- and S- arrival times from 227 earthquakes with gap $< 200^\circ$ were

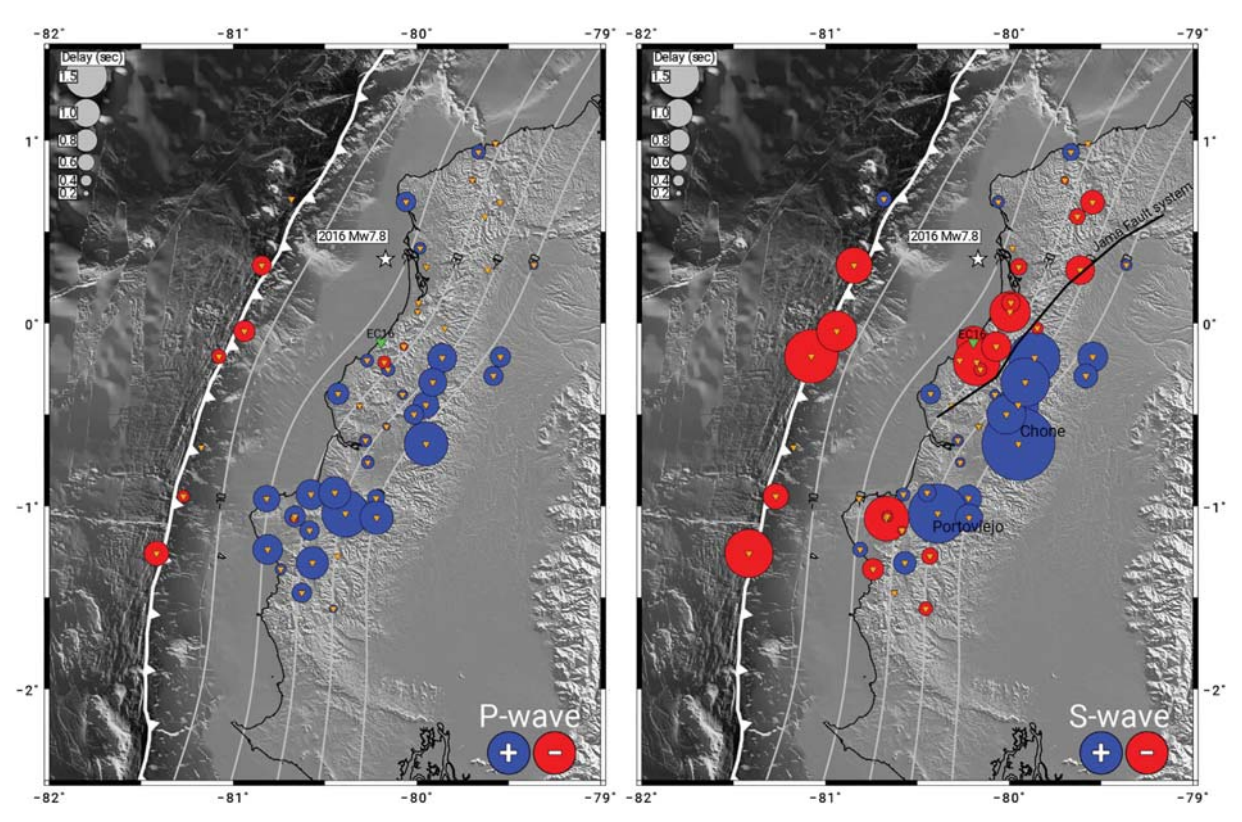


Fig. 8. Map with station corrections for P- (right) and S- (left) phases obtained after the 1D inversion. Inverted green triangle represents the reference station EC16. White star is showing the epicenter of the 2016 Mw 7.8 Pedernales earthquake. Inland and seafloor topography from Michaud et al. (2006). Trench data obtained from Collot et al. (2004). Slab 10 km depth contours from Hayes et al. (2012) are shown in gray lines. Jama Fault System (JFS) trace extracted from Reyes and Michaud (2012). (For interpretation of the references to color in this figure legend, the reader is referred to the web version of this article.)

inverted with VELEST to obtain absolute velocities, hypocentral locations and station correction terms.

The obtained minimum 1D velocity model shows a good resolution down to 40 km depth constrained with the ray paths and the earthquake distribution. The area has an average Vp/Vs ratio of 1.82 which varies with depth that may be related to hydration and serpentinization in the downgoing plate.

The seismicity is distributed in streaks which align perpendicular to the trench. Cross sections allow us to identify the seismogenic contact between the Nazca and South American plates. Shallow seismicity was observed in both northern and southern segments of the rupture area suggesting the activation of faults in the overriding plate. Some of the observed seismicity reached the trench which suggests the absence of a frontal accretionary prism.

Regional moment tensors were calculated to analyze the source mechanism of some events offshore. Although the majority of the events show focal mechanisms consistent with the subduction process, we also observe extensional faulting in the marine forearc that can be associated to the subduction of already-mapped seamounts. We also found strike-slip faulting which might be related to the reactivation of a strike-slip structure after the 2016 Mw 7.8 Pedernales earthquake that, in combination with the subduction of the crest of the CR, might cause the nucleation of the observed seismicity along the marine forearc margin. The observation of this type of activity suggests the need to reevaluate the geological structures in the marine forearc and to update the seismic hazard map for this region including the possible scenario of a large strike-slip event.

Acknowledgments

This study was supported by IGEPN, IRD, the INSU,CNRS and the ANR grant ANR-15-CE04-0004. The UK portion of the temporary

deployment was supported by NERC grant NE/P008828/1. The US portion of the temporary deployment was supported by IRIS PASSCAL and NSF RAPID Program Award EAR-1642498. SLR acknowledges partial support from Programa Formacion de Capital Humano Avanzado, BECAS DE DOCTORADO EN EL EXTRANJERO, BECAS CHILE (Grant 8068/2015). HAD acknowledges support from ANR project ANR-15-CE04-0004 and UCA/JEDI project ANR-15-IDEX-01.

We are also indebted to Ben Yates, Davide Oregioni and Deny Malengros from Geoazur laboratories, INOCAR, Comandante Andrès Pazmino (INOCAR) and Captain Patricio Estupinian (Esmeraldas Coastguard) to operate OBSs at sea in very harsh environments.

Authors want to thanks to all involved in the deployment and data collection for his invaluable collaboration with this study. Finally, to all the people in Ecuador who allowed us to install our stations in their houses, big thanks for your hospitality, patience and help when was needed.

Appendix A. Supplementary data

Supplementary data to this article can be found online at https://doi.org/10.1016/j.tecto.2019.228165.

References

Abe, K., 1979. Size of great earthquakes of 1837–1974 inferred from tsunami data. Journal of Geophysical Research: Solid Earth 84 (B4), 1561–1568.

Agudelo, W., Ribodetti, A., Collot, J.Y., Operto, S., 2009. Joint inversion of multichannel seismic reflection and wide-angle seismic data: improved imaging and refined velocity model of the crustal structure of the North Ecuador–South Colombia convergent margin. Journal of Geophysical Research: Solid Earth 114 (B2).

Agurto, H., Rietbrock, A., Barrientos, S., Bataille, K., Legrand, D., 2012. Seismo-tectonic structure of the Aysén Region, Southern Chile, inferred from the 2007 Mw = 6.2 Aysén earthquake sequence. Geophys. J. Int. 190 (1), 116–130.

Agurto-Detzel, H., Font, Y., Charvis, P., Régnier, M., Rietbrock, A., Ambrois, D., ... De

Barros, L., 2019. Ridge subduction and afterslip control aftershock distribution of the 2016 Mw 7.8 Ecuador earthquake. Earth Planet. Sci. Lett. 520, 63–76.

- Alvarado, A., Audin, L., Nocquet, J.M., Jaillard, E., Mothes, P., Jarrín, P., Cisneros, D., 2016. Partitioning of oblique convergence in the northern Andes subduction zone: migration history and the present-day boundary of the North Andean Sliver in Ecuador. Tectonics 35 (5), 1048–1065.
- Alvarado, A., Ruiz, M., Mothes, P., Yepes, H., Segovia, M., Vaca, M., Aguilar, J., 2018. Seismic, volcanic, and geodetic networks in Ecuador: building capacity for monitoring and research. Seismol. Res. Lett. 89 (2A), 432–439.
- Anderson, H., Webb, T., 1994. New Zealand seismicity: patterns revealed by the upgraded National Seismograph Network. N. Z. J. Geol. Geophys. 37 (4), 477–493.
- Araujo, S., 2016. Travel Time Tomography of the Crust and the Mantle Beneath Ecuador From Data of the National Seismic Network. (Doctoral dissertation, Grenoble Alpes).
- Asano, Y., Saito, T., Ito, Y., Shiomi, K., Hirose, H., Matsumoto, T., ... Sekiguchi, S., 2011. Spatial distribution and focal mechanisms of aftershocks of the 2011 off the Pacific coast of Tohoku Earthquake. Earth, Planets and Space 63 (7), 29.
- Bangs, N.L., McIntosh, K.D., Silver, E.A., Kluesner, J.W., Ranero, C.R., 2015. Fluid accumulation along the Costa Rica subduction thrust and development of the seismogenic zone. Journal of Geophysical Research: Solid Earth 120 (1), 67–86.
- Barnes, P.M., Lamarche, G., Bialas, J., Henrys, S., Pecher, I., Netzeband, G.L., Crutchley, G., 2010. Tectonic and geological framework for gas hydrates and cold seeps on the Hikurangi subduction margin, New Zealand. Mar. Geol. 272 (1–4), 26–48.
- Beauval, C., Yepes, H., Bakun, W.H., Egred, J., Alvarado, A., Singaucho, J.C., 2010. Locations and magnitudes of historical earthquakes in the Sierra of Ecuador (1587–1996). Geophys. J. Int. 181 (3), 1613–1633.
- Beck, S.L., Ruff, L.J., 1984. The rupture process of the great 1979 Colombia earthquake: evidence for the asperity model. J. Geophys. Res. 89, 9281–9291.
- Bilek, S.L., 2010. Invited review paper: Seismicity along the South American subduction zone: review of large earthquakes, tsunamis, and subduction zone complexity. Tectonophysics 495 (1–2), 2–14.
- Bloch, W., John, T., Kummerow, J., Salazar, P., Krüger, O.S., Shapiro, S.A., 2018.
 Watching dehydration: Seismic indication for transient fluid pathways in the oceanic mantle of the subducting Nazca Slab. Geochem. Geophys. Geosyst. 19 (9), 3189–3207.
- Bolton, P.A., 1991. Local Level Economic and Social Consequences. The March 5, 1987, Ecuador Earthquakes: Mass Wasting and Socioeconomic Effects. pp. 100.
- Bristow, C.R., Hoffstetter, R., Feininger, T., Hall, M.T., 1977. Léxico estratigráfico del Ecuador. CENTRE NATIONAL DE LA RECHERCHE SCIENTIFIQUE.
- Calahorrano, A., 2001. Estudio del origen del enjambre sismico de la zona norte de la ciudad de Quito, durante 1998–99. Escuela Politécnica Nacional, Facultad de Geologia, Minas y Petróleos, Quito, Ecuador Doctoral dissertation, Tesis de Ingeniera Geóloga.
- Calahorrano, A., Sallarès, V., Collot, J.Y., Sage, F., Ranero, C.R., 2008. Nonlinear variations of the physical properties along the southern Ecuador subduction channel: results from depth-migrated seismic data. Earth Planet. Sci. Lett. 267 (3–4), 453–467.
- Cano, L.C.G., Galve, A., Charvis, P., Marcaillou, B., 2014. Three-dimensional velocity structure of the outer fore arc of the Colombia-Ecuador subduction zone and implications for the 1958 megathrust earthquake rupture zone. Journal of Geophysical Research: Solid Earth 119 (2), 1041–1060.
- Cantalamessa, G., Di Celma, C., 2005. Sedimentary features of tsunami backwash deposits in a shallow marine Miocene setting, Mejillones Peninsula, northern Chile. Sediment. Geol. 178 (3–4), 259–273.
- Cantalamessa, G., Di Celma, C., Ragaini, L., Valleri, G., Landini, W., 2007. Sedimentology and high-resolution sequence stratigraphy of the late middle to late Miocene Angostura Formation (western Borbón Basin, northwestern Ecuador). J. Geol. Soc. 164 (3), 653–665.
- Chlieh, M., Mothes, P.A., Nocquet, J.M., Jarrin, P., Charvis, P., Cisneros, D., Vallée, M., 2014. Distribution of discrete seismic asperities and aseismic slip along the Ecuadorian megathrust. Earth Planet. Sci. Lett. 400, 292–301.
- Collings, R., Lange, D., Rietbrock, A., Tilmann, F., Natawidjaja, D., Suwargadi, B., Saul, J., 2012. Structure and seismogenic properties of the Mentawai segment of the Sumatra subduction zone revealed by local earthquake traveltime tomography. Journal of Geophysical Research: Solid Earth 117 (B1).
- Collot, J.Y., Charvis, P., Gutscher, M.A., Operto, S., 2002. Exploring the Ecuador-Colombia active margin and interplate seismogenic zone. EOS, Transactions American Geophysical Union 83 (17), 185–190.
- Collot, J.Y., Marcaillou, B., Sage, F., Michaud, F., Agudelo, W., Charvis, P., Spence, G., 2004. Are rupture zone limits of great subduction earthquakes controlled by upper plate structures? Evidence from multichannel seismic reflection data acquired across the northern Ecuador–southwest Colombia margin. Journal of Geophysical Research: Solid Earth 109 (B11).
- Collot, J.Y., Migeon, S., Spence, G., Legonidec, Y., Marcaillou, B., Schneider, J.L., Pazmino, A., 2005. Seafloor margin map helps in understanding subduction earthquakes. Eos, Transactions American Geophysical Union 86 (46), 463–465.
- Collot, J.Y., Michaud, F., Alvarado, A., Marcaillou, B., Sosson, M., Ratzov, G., ... Pazmino, A., 2009. Visión general de la morfología submarina del margen convergente de Ecuador-Sur de Colombia: implicaciones sobre la transferencia de masa y la edad de la subducción de la Cordillera de Carnegie. Geologia y Geofisica Marina y Terestre del Ecuador CNDM-INOCAR-IRD, PSE001-09, Guayaquil, Ecuador, pp. 47–74.
- Collot, J.Y., Sanclemente, E., Nocquet, J.M., Leprêtre, A., Ribodetti, A., Jarrin, P., ... Charvis, P., 2017. Subducted oceanic relief locks the shallow megathrust in central Ecuador. Journal of Geophysical Research: Solid Earth 122 (5), 3286–3305.
- Daly, M.C., 1989. Correlations between Nazca/Farallon plate kinematics and forearc basin evolution in Ecuador. Tectonics 8 (4), 769–790.
- Dorbath, L., Cisternas, A., Dorbath, C., 1990. Assessment of the size of large and great historical earthquakes in Peru. Bull. Seismol. Soc. Am. 80 (3), 551–576.

Egred, J., 1968. Breve historia sísmica de la República del Ecuador (1534 - 1565). Bol. Bibl. Geofís. Oceanogr. Am. 4 México.

- Ekström, G., Nettles, M., Dziewoński, A.M., 2012. The global CMT project 2004–2010: centroid-moment tensors for 13,017 earthquakes. Phys. Earth Planet. Inter. 200, 1–9.
- Farías, M., Comte, D., Roecker, S., Carrizo, D., Pardo, M., 2011. Crustal extensional faulting triggered by the 2010 Chilean earthquake: the Pichilemu Seismic Sequence. Tectonics 30 (6).
- Font, Y., Segovia, M., Vaca, S., Theunissen, T., 2013. Seismicity patterns along the Ecuadorian subduction zone: new constraints from earthquake location in a 3-D a priori velocity model. Geophys. J. Int. 193 (1), 263–286.
- Gailler, A., Charvis, P., Flueh, E.R., 2007. Segmentation of the Nazca and South American plates along the Ecuador subduction zone from wide angle seismic profiles. Earth Planet. Sci. Lett. 260 (3–4), 444–464.
- Graindorge, D., Calahorrano, A., Charvis, P., Collot, J.Y., Bethoux, N., 2004. Deep structures of the Ecuador convergent margin and the Carnegie Ridge, possible consequence on great earthquakes recurrence interval. Geophys. Res. Lett. 31 (4).
- Hacker, B.R., Abers, G.A., Peacock, S.M., 2003a. Subduction factory 1. Theoretical mineralogy, densities, seismic wave speeds, and H2O contents. Journal of Geophysical Research: Solid Earth 108 (B1).
- Hacker, B.R., Peacock, S.M., Abers, G.A., Holloway, S.D., 2003b. Subduction factory 2. Are intermediate-depth earthquakes in subducting slabs linked to metamorphic dehydration reactions? Journal of Geophysical Research: Solid Earth 108 (B1).
- Hayes, G.P., Wald, D.J., Johnson, R.L., 2012. Slab1.0: a three-dimensional model of global subduction zone geometries. Journal of Geophysical Research: Solid Earth (B1), 117.
- Hayes, G.P., Moore, G.L., Portner, D.E., Hearne, M., Flamme, H., Furtney, M., Smoczyk, G.M., 2018. Slab2, a comprehensive subduction zone geometry model. Science 362 (6410), 58–61.
- Herd, D.G., Youd, T.L., Meyer, H., Person, W.J., Mendoza, C., 1981. The Great Tumaco, Colombia earthquake of 12 December 1979. Science 211 (4481), 441–445.
- Hernández, M.J., Michaud, F., Rivadeneira, M., Barba, D., Collot, J.Y., 2011. El sistema de fallas de Jama en la plataforma continental (off-shore) del margen ecuatoriano: resultados preliminares a partir de la interpretación de perfiles sísmicos de reflexión.
- Hicks, S.P., Rietbrock, A., Ryder, I.M., Lee, C.S., Miller, M., 2014. Anatomy of a megathrust: the 2010 M8.8 Maule, Chile earthquake rupture zone imaged using seismic tomography. Earth Planet. Sci. Lett. 405, 142–155.
- Husen, S., Kissling, E., 2001. Postseismic fluid flow after the large subduction earthquake of Antofagasta, Chile. Geology 29 (9), 847–850.
- Husen, S., Kissling, E., Flueh, E., Asch, G., 1999. Accurate hypocentre determination in the seismogenic zone of the subducting Nazca Plate in northern Chile using a combined on-/offshore network. Geophys. J. Int. 138 (3), 687–701.
- IGEPN, 2016. informe sismico n18. https://www.igepn.edu.ec/servicios/noticias/1324-informe-sismico-especial-n-18-2016.
- Jaillard, E., Hérail, G., Monfret, T., Díaz-Martínez, E., Baby, P., Lavenu, A., Dumont, J.F., 2000. Tectonic evolution of the Andes of Ecuador, Peru, Bolivia and northernmost Chile. Tectonic Evolution of South America 31, 481–559.
- Kanamori, H., Given, J.W., 1981. Use of long-period surface waves for rapid determination of earthquake-source parameters. Phys. Earth Planet. Inter. 27 (1), 8–31.
- Kanamori, H., McNally, K.C., 1982. Variable rupture mode of the subduction zone along the Ecuador-Colombia coast. Bull. Seismol. Soc. Am. 72 (4), 1241–1253.
- Kato, A., Iidaka, T., Ikuta, R., Yoshida, Y., Katsumata, K., Iwasaki, T., Watanabe, T., 2010.
 Variations of fluid pressure within the subducting oceanic crust and slow earth-quakes. Geophys. Res. Lett. 37 (14).
- Kato, A., Sakai, S.I., Obara, K., 2011. A normal-faulting seismic sequence triggered by the 2011 off the Pacific coast of Tohoku Earthquake: wholesale stress regime changes in the upper plate. Earth, planets and space 63 (7), 43.
- Kelleher, J.A., 1972. Rupture zones of large South American earthquakes and some predictions. J. Geophys. Res. 77 (11), 2087–2103.
- Kendrick, E., Bevis, M., Smalley Jr., R., Brooks, B., Vargas, R.B., Lauria, E., Fortes, L.P.S., 2003. The Nazca–South America Euler vector and its rate of change. J. S. Am. Earth Sci. 16 (2), 125–131.
- Kissling, E., Ellsworth, W.L., Eberhart-Phillips, D., Kradolfer, U., 1994. Initial reference models in local earthquake tomography. Journal of Geophysical Research: Solid Earth 99 (B10), 19635–19646.
- Lange, D., Tilmann, F., Barrientos, S.E., Contreras-Reyes, E., Methe, P., Moreno, M., Beck, S., 2012. Aftershock seismicity of the 27 February 2010 Mw 8.8 Maule earthquake rupture zone. Earth Planet. Sci. Lett. 317, 413–425.
- Lanning, F., Haro, A.G., Liu, M.K., Monzón, A., Monzón-Despang, H., Schultz, A., ... Vera-Grunauer, X., 2016. EERI Earthquake Reconnaissance Team Report: M7. 8 Muisne, Ecuador Earthquake on April 16. pp. 2016.
- Lee, W.H.K., Lahr, J.C., 1972. HYPO71: A Computer Program for Determining Hypocenter, Magnitude, and First Motion Pattern of Local Earthquakes (No. 72-224). US Geological Survey.
- León-Ríos, S., Ruiz, S., Maksymowicz, A., Leyton, F., Fuenzalida, A., Madariaga, R., 2016. Diversity of the 2014 Iquique's foreshocks and aftershocks: clues about the complex rupture process of a Mw 8.1 earthquake. J. Seismol. 20 (4), 1059–1073.
- Litherland, M. (1994). The metamorphic belts of Ecuador. British Geological Survey, Overseas Memoir., 11.
- Lonsdale, P., 2005. Creation of the Cocos and Nazca plates by fission of the Farallon plate. Tectonophysics 404 (3), 237–264.
- Luzieux, L.D.A., Heller, F., Spikings, R., Vallejo, C.F., Winkler, W., 2006. Origin and Cretaceous tectonic history of the coastal Ecuadorian forearc between 1 N and 3 S: paleomagnetic, radiometric and fossil evidence. Earth Planet. Sci. Lett. 249 (3–4), 400–414.
- Marcaillou, B., Spence, G., Collot, J.Y., Wang, K., 2006. Thermal regime from bottom simulating reflectors along the North Ecuador–south Colombia margin: relation to

- margin segmentation and great subduction earthquakes. Journal of Geophysical Research: Solid Earth 111 (B12).
- Marcaillou, B., Collot, J.Y., Ribodetti, A., d'Acremont, E., Mahamat, A.A., Alvarado, A., 2016. Seamount subduction at the North-Ecuadorian convergent margin: effects on structures, inter-seismic coupling and seismogenesis. Earth Planet. Sci. Lett. 433, 146–158.
- Meissnar, R.O., Flueh, E.R., Stibane, F., Berg, E., 1976. Dynamics of the active plate boundary in Southwest Colombia according to recent geophysical measurements. Tectonophysics 35 (1–3), 115–136.
- Meltzer, A., Beck, S., Ruiz, M., Hoskins, M., Soto-Cordero, L., Stachnik, J.C., ... Mercerat, E.D., 2019. The 2016 Mw 7.8 Pedernales Earthquake. Seismological Research Letters RAPID Response Deployment, Ecuador.
- Mendoza, C., Dewey, J.W., 1984. Seismicity associated with the great Colombia-Ecuador earthquakes of 1942, 1958, and 1979: implications for barrier models of earthquake rupture. Bull. Seismol. Soc. Am. 74 (2), 577–593.
- ed. a. Ř. d. E.P. c. y. t. d. INOCARMichaud, F., Collot, J.Y., Alvarado, A., Lopez, E., 2006).

 Batimetría y Relieve Continental. IOA-CVM-02-Post, INOCAR, Guayaquil, Ecuador, pp. 679.
- Michaud, F., Proust, J.N., Collot, J.Y., Lebrun, J.F., Witt, C., Ratzov, G., Penafiel, L., 2015.Quaternary sedimentation and active faulting along the Ecuadorian shelf: preliminary results of the ATACAMES Cruise (2012). Mar. Geophys. Res. 36 (1), 81–98.
- Mothes, P.A., Nocquet, J.M., Jarrín, P., 2013. Continuous GPS network operating throughout Ecuador. Eos, Transactions American Geophysical Union 94 (26), 229–231.
- Nocquet, J.M., Jarrin, P., Vallée, M., Mothes, P.A., Grandin, R., Rolandone, F., Régnier, M., 2017. Supercycle at the Ecuadorian subduction zone revealed after the 2016 Pedernales earthquake. Nat. Geosci. 10 (2), 145.
- Pasten-Araya, F., Salazar, P., Ruiz, S., Rivera, E., Potin, B., Maksymowicz, A., et al., 2018. Fluids along the plate interface influencing the frictional regime of the Chilean Subduction zone, northern Chile. Geophys. Res. Lett. 45. https://doi.org/10.1029/2018GI.079283.
- Peacock, S.M., 2001. Are the lower planes of double seismic zones caused by serpentine dehydration in subducting oceanic mantle? Geology 29 (4), 299–302.
- Pilger, R.H., 1984. Cenozoic plate kinematics, subduction and magmatism: South American Andes. J. Geol. Soc. 141 (5), 793–802.
- Reyes, P., Michaud, F., 2012. Mapa Geologico de la Margen Costera Ecuatoriana (1500000). EPPetroEcuador-IRD, Ouito Ecuador.
- Ramirez, J.E., 1968. Historia de los terremotos en Colombia. Bol. Bibliog. (IPGH), Geof. Ocen. Am. 14, 1–146 (1965/1967).
- Rietbrock, A., Ryder, I., Hayes, G., Haberland, C., Comte, D., Roecker, S., Lyon-Caen, H., 2012. Aftershock seismicity of the 2010 Maule Mw = 8.8, Chile, earthquake: Correlation between co-seismic slip models and aftershock distribution? Geophys. Res. Lett. 39 (8).
- Rolandone, F., Nocquet, J.M., Mothes, P.A., Jarrin, P., Vallée, M., Cubas, N., Font, Y., 2018. Areas prone to slow slip events impede earthquake rupture propagation and promote afterslip. Sci. Adv. 4 (1), eaao6596.
- Rothé, J.P., 1969. The Seismicity of the Earth, 1953–1965: La Séismicité Du Globe 1953, 1965. Unesco.
- Ruiz, S., Metois, M., Fuenzalida, A., Ruiz, J., Leyton, F., Grandin, R., Campos, J., 2014. Intense foreshocks and a slow slip event preceded the 2014 Iquique Mw 8.1 earth-quake. Science 345 (6201), 1165–1169.
- Ruiz, S., Klein, E., del Campo, F., Rivera, E., Poli, P., Metois, M., Madariaga, R., 2016. The seismic sequence of the 16 September 2015 Mw 8.3 Illapel, Chile, earthquake. Seismol. Res. Lett. 87 (4), 789–799.
- Ryder, I., Rietbrock, A., Kelson, K., Bürgmann, R., Floyd, M., Socquet, A., Carrizo, D.,

- 2012. Large extensional aftershocks in the continental forearc triggered by the 2010 Maule earthquake, Chile. Geophys. J. Int. 188 (3), 879–890.
- Sallarès, V., Charvis, P., 2003. Crustal thickness constraints on the geodynamic evolution of the Galapagos Volcanic Province. Earth Planet. Sci. Lett. 214 (3-4), 545-559.
- Sallarès, V., Charvis, P., Flueh, E.R., Bialas, J., SALIERI Scientific Party, 2005. Seismic structure of the Carnegie ridge and the nature of the Galapagos hotspot. Geophys. J. Int. 161 (3), 763–788.
- Segovia, M., 2001. El sismo de Bahía del 4 de agosto de 1998: Caracterización del mecanismo de ruptura y análisis de la sismicidad en la zonacostera. In: Titulo de Ingeniera Geologia (tesis): Escuela Politecnica Nacional, Quito, Ecuador.
- Segovia, M., Alvarado, A., Collot, J.Y., Sallares, V., Pazmiño, N., 2009. Breve análisis de la sismicidad y del campo de esfuerzos en el Ecuador. In: Geología y Geofísica Marina y Terrestre del Ecuador: desde la costa continental hasta las Islas Galápagos, pp. 131–149
- Segovia, M., Font, Y., Regnier, M.M., Charvis, P., Nocquet, J.M., Galve, A., ... Ruiz, M.C., 2015. Intense microseismicity associated with a SSE at La Plata Island in the central subduction zone of Ecuador. In: AGU Fall Meeting Abstracts, (December).
- Sennson, J.L., Beck, S.L., 1996. Historical 1942 Ecuador and 1942 Peru subduction earthquakes and earthquake cycles along Colombia-Ecuador and Peru subduction segments. Pure Appl. Geophys. 146 (1), 67–101.
- Sokos, E.N., Zahradník, J., 2008. ISOLA a Fortran code and a Matlab GUI to perform multiple-point source inversion of seismic data. Comput. Geosci. 34 (8), 967–977.
- Sokos, E., Zahradník, J., 2013. Evaluating centroid-moment-tensor uncertainty in the new version of ISOLA software. Seismol. Res. Lett. 84 (4), 656–665.
- Storchak, D.A., Di Giacomo, D., Bondár, I., Engdahl, E.R., Harris, J., Lee, W.H.K., Villaseñor, A., Bormann, P., 2013. Public Release of the ISC-GEM Global Instrumental Earthquake Catalogue (1900-2009). Seism. Res. Lett. 84 (5), 810–815. https://doi. org/10.1785/0220130034.
- Toda, S., Tsutsumi, H., 2013. Simultaneous reactivation of two, subparallel, inland normal faults during the Mw 6.6 11 April 2011 Iwaki earthquake triggered by the Mw 9.0 Tohoku-Oki, Japan, earthquake. Bull. Seismol. Soc. Am. 103 (2B), 1584–1602.
- Vaca, S., 2017. Interaction Between Tectonics, Slow-slip Processes and Earthquake Mechanisms across the North Andean Sliver (Ecuador). Thèse de doctorat de Sciences de la Terre et de l'environnement. INSTITUT DE PHYSIQUE DU GLOBE DE PARIS
- Vaca, S., Régnier, M., Bethoux, N., Alvarez, V., Pontoise, B., 2009. Sismicidad de la región de Manta: Enjambre sísmico de Manta-2005. In: Geologia y Geofisica Marina y Terrestre del Ecuador Desde la Costa Continental Hasta las Islas Gapapagos, pp. 151-166.
- Vaca, S., Vallée, M., Nocquet, J.M., Battaglia, J., Régnier, M., 2018. Recurrent slow slip events as a barrier to the northward rupture propagation of the 2016 Pedernales earthquake (Central Ecuador). Tectonophysics 724, 80–92.
- Vallée, M., Nocquet, J.M., Battaglia, J., Font, Y., Segovia, M., Regnier, M., ... Yepes, H., 2013. Intense interface seismicity triggered by a shallow slow slip event in the Central Ecuador subduction zone. Journal of Geophysical Research: Solid Earth 118 (6), 2965–2981.
- Wadati, K., Oki, S., 1933. On the travel time of earthquake waves. (Part II). Journal of the Meteorological Society of Japan. Ser. II 11 (1), 14-28.
- White, S.M., Trenkamp, R., Kellogg, J.N., 2003. Recent crustal deformation and the earthquake cycle along the Ecuador–Colombia subduction zone. Earth Planet. Sci. Lett. 216 (3), 231–242.
- Yoshimoto, M., Kumagai, H., Acero, W., Ponce, G., Vásconez, F., Arrais, S., ... Chamorro, O., Research Letters, Geophysical, 2017. Depth-dependent rupture mode along the Ecuador-Colombia subduction zone. Geophys. Res. Lett. 44 (5), 2203–2210.